# Non-destructive 3D pathology with analysis of nuclear features for prostate cancer risk assessment

**Robert Serafin**
University of Washington    https://orcid.org/0000-0002-6646-353X

**Can Konyuncu**
Georgia Institute of Technology and Emory University

**Weisi Xie**
University of Washington

**Hongyi Huang**
University of Washington

**Adam Glaser**
University of Washington

**Nicholas Reder**
University of Washington

**Andrew Janowczyk**
Case Western Reserve University

**Lawrence True**
University of Washington

**Anant Madabhushi**
Georgia Institute of Technology and Emory University

**Jonathan Liu** ( ✉ jonliu@uw.edu )
University of Washington    https://orcid.org/0000-0001-5650-3086

**Article**

**Keywords:**

# Abstract

Prostate cancer treatment decisions are heavily reliant upon the subjective visual interpretation (assigning Gleason patterns, or ISUP grade groups) of limited numbers of 2D histology sections. Under this paradigm, inter-observer variance is high, with ISUP grades not correlating well with the outcomes of individual patients, which contributes to the over- and under-treatment of patients. Recent studies have demonstrated improved prognostication of prostate cancer outcomes based on computational analyses of glands and nuclei within 2D whole slide images. Our group has also shown that the computational analysis of 3D glandular features, extracted from 3D pathology datasets of whole intact biopsies, can allow for improved recurrence prediction compared to corresponding 2D features. Here we seek to expand on these prior studies by exploring the prognostic value of 3D shape-based nuclear features in prostate cancer (e.g., nuclear size, sphericity). 3D pathology datasets were generated with open-top light-sheet (OTLS) microscopy of 102 cancer-containing biopsies extracted *ex vivo* from the prostatectomy specimens of n = 46 patients. A deep learning-based segmentation workflow for 3D nuclear segmentation and 3D glandular segmentation was used to segment nuclei within the glandular epithelium vs. stromal regions of the biopsies. 3D shape-based nuclear features were extracted, and a nested cross-validation scheme was used to train a supervised machine classifier based on 5-year biochemical recurrence (BCR) outcomes. Nuclear features of the glandular epithelium were found to be more prognostic than stromal cell nuclear features (AUC = 0.72 vs. 0.63). 3D shape-based nuclear features of the glandular epithelium were also more strongly associated with risk of BCR than analogous 2D features (AUC = 0.72 vs. 0.62). The results of this preliminary investigation suggest that 3D shape-based nuclear features are associated with prostate cancer aggressiveness and could be of value for the development of decision-support tools.

# Introduction

Prostate cancer (PCa) represents 1 in 8 of the newly detected cancer cases in the United States, affecting nearly 250,000 patients annually[1]. Currently, grading of PCa for prognosis and treatment planning relies on 2D histology, where a set of core-needle biopsies is formalin-fixed and paraffin-embedded (FFPE), sectioned, and mounted on glass slides for microscopic analysis. To assess the aggressiveness of the cancer, pathologists rely on the ISUP grade group system[2–4] which involves visual examination and interpretation of complex glandular morphologies in a limited number of 2D histological tissue sections (4-μm thick) cut from each biopsy. In this workflow, typically ~ 1% of the volumetric extent of each biopsy is analyzed. In part due to this limited "sampling" of the biopsies in 2D, grading of prostate cancer suffers from high levels of inter- and intra-observer variability[5–8]. A related issue is that ISUP grade groups do not precisely correlate with individual patient outcomes, especially for moderate-risk cases (ISUP Grade Group 2) that account for approximately 50% of the newly detected PCa cases in the United States. These problems contribute to the overtreatment of indolent cases (with surgery or radiation), which are often accompanied by life-changing side effects (incontinence or impotence) and avoidable healthcare costs. Conversely, they also contribute to the undertreatment of aggressive cases (with active surveillance), which can lead to potentially avoidable metastasis and death[9].

By combining recent advances in tissue-clearing techniques[10–12] and high-throughput three-dimensional microscopy[13–19], there is now the ability to generate non-destructive 3D pathology datasets of large clinical specimens (surgical excisions or whole biopsies). Unlike conventional histology, non-destructive 3D pathology achieves orders-of-magnitude greater microscopic sampling of excised tissues than conventional slide-based histology and enables volumetric quantification of diagnostically significant microarchitectures. The non-destructive imaging process also preserves tissue specimens for downstream molecular assays[20]. However, since a single 3D pathology dataset of a biopsy can be tens to hundreds of gigabytes in size, there are significant challenges for the human visual interpretation of such datasets. Manual examination of these datasets can be tedious, which motivates the development of computational methods for analysis. Here, we employ interpretable "hand-crafted" features, derived from segmentation masks of tissue structures (e.g., glands and nuclei), to facilitate the clinical acceptance of 3D pathology as a new diagnostic approach.

A recent study by our group demonstrated the benefits of the computational analysis of 3D glandular features for PCa risk stratification[19]. In that study, *ex vivo* biopsies were extracted from archived radical prostatectomy specimens obtained from patients with known 5-year biochemical recurrence (BCR) outcomes. These patients were originally diagnosed with low- to moderate-risk PCa (Grade Groups 1–3), with 50% of cases exhibiting BCR within 5 years of prostatectomy[21]. Biopsies were stained with small-molecule fluorescent analogs of hematoxylin and eosin (H&E), optically cleared with a dehydration and solvent-immersion protocol, and then non-destructively imaged with open-top light-sheet microscopy (OTLS) to generate whole-biopsy 3D pathology datasets (Fig. 1A). For 3D segmentation of prostate glands (lumen, epithelium, and stromal compartments), our group developed a computational pipeline called "image-translation-assisted segmentation in 3D" (ITAS3D). 3D glandular features (e.g., gland curvature, eccentricity, volume ratios) were extracted from the cancer-containing regions of the biopsies. We showed that these features are more strongly associated with BCR outcomes than analogous 2D glandular features.

In addition to glandular morphologies, which are currently relied upon for Gleason grading (ISUP Grade Groups), studies using 2D whole-slide images (conventional 2D pathology) have shown that there is prognostic value in examining nuclear features within PCa [20–33]. It is also known that changes in nuclear structure can reflect the underlying molecular alterations within diseases[29–33]. However, the prognostic value of 3D nuclear features has not been previously reported. Therefore, we sought to quantify a preliminary set of 3D shape-based nuclear features and their 2D counterparts to directly compare their ability to predict BCR outcomes. Our underlying hypothesis is that 2D cross sections of a nucleus (as seen with conventional histology) cannot fully elucidate certain complex changes in 3D nuclear morphology and are therefore less prognostically informative. For example, **Supplementary Fig. 1** provides a simple illustration of how an irregularly shaped 3D nucleus may appear quite regular and circular when viewed as 2D cross sections.

For 3D nuclear and glandular segmentation, we utilized cellpose[34] and our previously reported ITAS3D pipeline[19], respectively, which allowed us to distinguish between nuclei within the gland epithelium vs. surrounding stromal compartments (Fig. 1B). 3D shape-based nuclear features (i.e., spatial metrics) and analogous 2D nuclear features were extracted from each biopsy, such that the prognostic value of 3D vs. 2D nuclear features could be compared. These 3D and 2D features were used to train a multi-parameter machine classifier to stratify patients based on their BCR outcomes, which serves as a proxy for aggressive vs. indolent PCa (Fig. 1C).

# Materials And Methods

# Collection and processing of simulated biopsies from archived tissues

This study was approved by the institutional review board (IRB) of the University of Washington (Seattle, WA; Study 00004980), where research specimens were previously obtained from patients with informed consent. Archived FFPE prostatectomy specimens from a prior case-cohort research study (Canary TMA)[21] were collected from 50 patients with PCa, all of which were identified as ISUP Grade Group 1−3 (Gleason Grade 3 + 3, 3 + 4, or 4 + 3). These patients were followed for at least 5 years after radical prostatectomy as part of the prior study[21], in which the primary study endpoints were 5-year BCR outcomes and time to BCR, which were also used as endpoints for this study. FFPE specimens were identified for each case corresponding to the six regions of the prostate targeted in standard biopsy procedures (Fig. 1A). The identified specimens were deparaffinized by heating them at 75 C for 1 hour until the paraffin wax melted. The specimens were then placed in 65 C xylene for 48 hours. Next, a simulated core-needle biopsy (~ 1mm in width) was taken from each of the six deparaffinized blocks per case, resulting in 300 total biopsy cores (Fig. 1A).

We used a previously developed "T&E" staining protocol (nuclear dye TO-PRO3 and Eosin) and imaged each biopsy core using OTLS microscopy[15,19]. Simulated biopsies underwent two 1-hour washes in 100% ethanol to remove excess xylene and were partially rehydrated in 70% ethanol for 1 hour. Individual biopsies were stained for 48 hours in 70% ethanol at pH 4 with a 1:200 dilution of Eosin-Y and a 1:500 dilution of TO-PRO3 at room temperature with light agitation. After staining was complete, the biopsies were dehydrated in 100% ethanol for 2 hours. Samples were optically cleared by individually placing them in ethyl cinnamate (refractive index of n = 1.56) for 8 hours before imaging them with OTLS microscopy.

During imaging, ethyl cinnamate (n = 1.56) was used as the immersion medium and samples mounted within a custom HIVEX (n = 1.55) biopsy holder, as described previously[15]. A four-channel digitally controlled laser package (Skyra, Cobolt Lasers) was used for illumination. TO-PRO3 fluorescence was excited at 638 nm and Eosin fluorescence was excited at 561 nm. Fluorescence bandpass filters at 721 nm +/- 65 nm and 618 nm +/- 50 nm were used for collection of TO-PRO3 fluorescence and Eosin fluorescence, respectively. The lateral and axial resolution of the OTLS microscope used for this study

was ~ 0.95 microns and 3.5 microns, respectively (full width at half maximum of the point spread function). Tissues were imaged at an isotropic sampling pitch of ~ 0.44 μm/pixel. The volumetric imaging time was approximately 0.5 minute per cubic mm of tissue for each illumination wavelength.

## Data preparation

Two-channel OTLS microscopy datasets were stored on disk in the HDF5 format with metadata in an XML file. A custom compression filter (B3D) was used to provide 10x lossless compression. Raw OTLS images were reviewed in BigDataViewer[35] by board-certified pathologists to identify cancer-containing biopsies (Fig. 1A). Of the initial 300 biopsy cores extracted, 118 contained cancer. Upon review, 102 of the cancer-containing biopsies from a 46-patient cohort had sufficient data quality for 3D nuclear segmentation. Visual examination of the 3D datasets enabled us to identify regions of the biopsies in which most of the glands were cancer. Continuous (stitched and fused) 3D volumes were created of these cancer regions using the Image-J BigStitcher plugin[36]. False coloring was performed to achieve an H&E-like appearance to our OTLS datasets using a previously published method that mimics Beer-Lambert law absorption of light as a function of staining concentration [37].

## Nuclear segmentation and feature extraction

Given the memory requirements necessary for 3D segmentation, fused 3D images were broken into discrete chunks for processing. Each data chunk was 2048 x 1432 x 500 voxels in size, or approximately 1024 microns by 716 microns by 200 microns in the axial direction (along the length of the needle core) (Fig. 2A, B). To prepare the images for segmentation, data chunks underwent median filtering with a circular structuring element (r = 2 voxels) from *scikit-image*[38] followed by contrast-limited adaptive histogram equalization (CLAHE) (Fig. 2C, **Supplementary Fig. 5**). After preprocessing, data chunks were passed into the cellpose[34] 3D nuclear segmentation model using an average diameter of 17 voxels, net averaging, and a batch size of 6 as the input parameters (Fig. 2D). 3D segmentation masks (instance segmentation) were saved to disk. All processing was done on a desktop computer equipped with 512 GB of RAM and a Nvidia Quadro 5000 RTX GPU.

Prior to feature extraction, segmented nuclei that touched the boundaries of each data chunk were cleared using the *clear_border* method from the *skimage.segmentation* python library[38]. Within each segmented data chunk, small objects measuring less than the 1st percentile in total volumetric extent were also removed as noise. Quantitative features were extracted from the segmentation masks using the *regionprops* method from the *skimage.measure* python library. A full set of 3D nuclear features (and 2D counterparts) used in this study is listed in **Supplementary Fig. 2**. The glandular masks of each cancerous region, generated via our previous ITAS3D pipeline[19], were used to classify segmented nuclei as belonging to epithelial or stromal tissue compartments based on the centroid location of each segmented nucleus within the glandular mask. Biopsy-level feature sets were collected by averaging the extracted features from all data chunks within a biopsy.

To compare the prognostic value of 2D and 3D nuclear features, 2D nuclear features were extracted from the 3D dataset at three cross-sectional levels separated by 20 μm, and then averaged (**Supplementary Fig. 3**). This replicates the standard-of-care pathology practice at many institutions in which histology sections are cut (and viewed) at three such levels[39].

# Correlation between nuclear features and BCR outcomes

Patients who experienced BCR within 5 years after radical prostatectomy are referred to as the 'BCR' group, and all other patients are referred to as 'non-BCR.' Here, biochemical recurrence (BCR) is defined as a rise in prostate-specific antigen (PSA) levels of > 0.2 ng/mL after treatment (> 8 weeks after radical prostatectomy). To assess the ability of different nuclear features to distinguish between BCR and non-BCR groups, we applied ROC analysis from which the area-under-the-curve (AUC) could be extracted.

Using the binary 5-year BCR category as the endpoint, a multiparameter classifier was developed to stratify patient risk. The least absolute shrinkage and selection operator (LASSO) linear regression model was used[40]. LASSO minimizes overfitting by making use of an L1 regularization term and identifies a subset of the most predictive input features. The LASSO tuning parameter $\lambda$ was optimized using an internal 4-fold cross validation (CV) scheme, where the dataset was randomly separated into four equally sized groups: three training datasets, and one to validate the model's performance. Due to the lack of an external validation cohort, a nested CV scheme was used to determine the performance of the multiparameter models without bias or data leakage between parameter estimation and validation. Hyperparameter tuning was performed during each iteration of the outer CV, and LASSO regression was applied on the training set of the outer CV once an optimal $\lambda$ was identified in the inner CV. AUC values were calculated from the validation dataset of the outer CV. This nested CV was performed 200 times to determine an AUC (average and SD)[41]. The exact same nested CV scheme was used to develop multiparameter classifiers based on 3D and 2D nuclear features.

Kaplan-Meier (KM) analysis was carried out to compare BCR-free survival rates for high- vs. low-risk groups of patients. This analysis used a subset of 45 cases for which time-to-recurrence data is available. The performance of the models based on 2D or 3D features for epithelial nuclei was quantified with *p*-values (via log-rank test), hazard ratios (HR), and concordance index (C-index) metrics. For the multiparameter classification model used for KM analysis, the outer 4-fold CV in our nested CV schema was replaced by a leave-one-out approach, where one case was left out each iteration (45 total iterations, i.e. one iteration for each of the cases) to calculate the probability of 5-year BCR for that patient[42]. The samples were labeled as low- or high-risk via a posterior class probability threshold of 0.5. MATLAB was used for KM analysis and all other statistical analyses was performed in Python using the *scipy* and *scikit-learn* libraries[43].

# Results

# 3D nuclear segmentation

Generating ground-truth annotations to train a 3D nuclear segmentation algorithm can be tedious and challenging. Therefore, we chose cellpose as our segmentation framework for two reasons: 1) as a "generalist" segmentation algorithm, cellpose requires minimal to no retraining or annotations to operate on unseen data, 2) cellpose is compatible with 3D datasets, and can efficiently segment densely packed nuclei within large tissue volumes. To assess segmentation quality, we generated 3D ground truth annotations of nuclei within small sub-volumes (n = 6) of PCa biopsies imaged with OTLS microscopy and found that cellpose successfully generated 3D nuclear segmentations with an average dice coefficient of 0.81 (**Supplementary Fig. 4**). When evaluating the results of the cellpose 3D nuclear segmentation model on our moderate-resolution OTLS datasets (~ 0.9-micron lateral resolution), the best segmentation results were achieved without down sampling our datasets (**Supplementary Video 2**).

At full resolution, each individual (single biopsy) 3D pathology dataset was too large to segment at once. Thus, cancerous biopsy regions were divided into smaller chunks for 3D segmentation (Fig. 2A, B). Each data chunk underwent a two-step preprocessing routine (Fig. 2C) (see materials and methods, **Supplementary Fig. 5**) that improved segmentation quality. This process decreased the rate of over-segmentation and improved the detection of nuclei in low-signal regions of the tissue. Images were then passed into the cellpose nuclear-segmentation model to generate a final 3D segmentation mask (Fig. 2-D, **Supplementary Videos 1 & 3**). An example image atlas of 3D nuclear segmentation results, and morphological separation of nuclei (epithelial and stromal compartments) using ITAS3D generated glandular segmentation is shown in Fig. 3.

# Preliminary clinical study: correlating 3D nuclear features with BCR outcomes

To evaluate the prognostic value of 3D vs. 2D nuclear features (see materials and methods), our study consisted of 46 PCa cases in which the patients were followed for a minimum of 5 years after radical prostatectomy as part of the Canary TMA case-cohort study, which recruited primarily low- to intermediate-risk patients[21]. The primary endpoints of the Canary TMA study were 5-year biochemical recurrence (BCR) outcomes and time to BCR, which were also used as endpoints in our study here. Roughly half of the cases in the Canary TMA study had BCR within 5 years.

For each case, archived FFPE tissue blocks were identified from the six regions of the prostate that are biopsied by urologists when performing standard sextant biopsy procedures. Next, a simulated core needle biopsy was extracted from each of the six FFPE blocks per patient (n = 276 total biopsy cores). The biopsies were deparaffinized, labeled with fluorescent analogs of H&E, optically cleared, and imaged with an OTLS microscope (see materials and methods). Review of the 3D pathology datasets by genitourinary pathologists (L.D. True and N.P. Reder) identified 102 cancer-containing biopsies, along with axial coordinates of the regions within each of those biopsies in which most glands were cancerous. The nuclear-segmentation and ITAS3D (gland-segmentation) pipelines were applied to the cancerous regions of all 102 cancer-containing biopsies. By combining the 3D nuclear segmentations (instance segmentations) with the glandular segmentation masks (semantic segmentation), nuclei were identified

as contained in either the glandular epithelium or stromal tissue compartments (see Materials and Methods).

2D and 3D shape-based nuclear features were quantified and analyzed in terms of their association with BCR outcomes (see **Supplementary Fig. 2** for the full list of features). For 2D analysis, average values from a total of 3 cross-sectional levels were calculated, in which the three levels were separated by 20 μm (mimicking clinical practice at many institutions, see **Supplementary Fig. 3**). A total of 18 shape-based nuclear features were used as the inputs into a multiparameter risk classifier based on 5-year BCR outcomes. Separate models were trained for the nuclei in the glandular epithelium vs. stromal compartments. The average area-under-the-ROC-curve (AUC) was used as a measure of the ability of the combined nuclear features to predict 5-year BCR outcomes as a proxy for indolent vs. aggressive disease.

3D shape-based nuclear features consistently outperform their analogous 2D features, both for epithelial nuclei and stromal nuclei (Fig. 4A, B). When comparing Fig. 4A and Fig. 4B, it is apparent there is better performance with models trained on shape-based nuclear features from the glandular epithelium than models trained with nuclei form the stromal regions. 3D shape-based nuclear features in the stroma are found to be weakly prognostic with an average AUC = 0.63 ± 0.06, while 2D shape-based nuclear features in the stroma are not prognostic with an average AUC = 0.50 ± 0.05.

Kaplan-Meier (KM) curves of BCR-free survival were constructed for a subset of cases in which time-to-recurrence (BCR) data was available (Fig. 4C, D). Compared with models based on 2D shape-based nuclear features, models based on 3D shape-based nuclear features are associated with a higher HR and C-index, along with a significant $P$ value ($P < 0.05$). This suggests a stronger association with outcome for 3D shape-based nuclear features compared to corresponding 2D features.

For this early-stage study, 14 out of 18 of the shape-based nuclear features were independently associated with BCR outcomes (p < 0.05). Of these 14 features, 5 were prognostically significant in 3D but not in 2D. As one example, Fig. 4E, F shows the mean and variance of the nucleus-to-convex hull ratio of epithelial nuclei (3D vs. 2D). The convex hull is the minimum polyhedron (or polygon in 2D) that encloses a nucleus. Figure 4E shows that the nuclei in BCR cases (i.e., aggressive PCa) typically have a higher mean nucleus-to-convex-hull ratio ($P = 1.1$ x $10^{-4}$). Physically, this means that the nuclei are more spherical or ovaloid rather than irregular and/or curved in shape. However, this relationship is not apparent in the 2D case ($P = 0.24$). Similarly, Fig. 4F demonstrates that the variance of the nucleus-to-convex-hull ratio is greater for recurrent vs. non-recurrent cases when examined in 3D with $P = 8.6$ x $10^{-6}$, while this difference is less in 2D ($P = 0.47$).

Overall, our analysis of a variety of nuclear shape features consistently reveals less heterogeneity (variance) in aggressive (BCR) cancers compared to non-aggressive cases (**Supplementary Fig. 6**). This parallels the results of a previous study in which higher-grade PCa cases had smaller and more homogeneous glandular structures (less spatial variance)[19].

# Discussion

Improvements in resolution, scale, and multiplexing capacity for non-destructive 3D imaging technologies are leading to new disease insights that can inform treatment decisions[20]. However, given the growing size of datasets generated by modern "spatial biology" techniques, computational tools must also be developed to enable pathologists and oncologists to efficiently comprehend such large datasets. An attractive initial approach is to rely on intuitive features familiar to pathologists (e.g. glandular and nuclear features), which will improve interpretability and facilitate clinical acceptance. As in our previous study using 3D glandular features[19], our goal in this study has been to demonstrate the value of 3D pathology by providing a direct comparison of intuitive 3D vs. 2D nuclear features analyzed computationally. Our work leverages the fact that computational 2D pathology has already been demonstrated to improve disease prognostication [28,44,45], and explores the additional value that computational 3D pathology can offer for certain applications such as risk stratification of PCa.

In this preliminary study, we have avoided comparing the analysis of our computationally derived 3D and 2D nuclear features with risk classifiers or nomograms that rely on human interpretation of 2D histology images[42,46,47]. Our motivation for this is that by directly comparing 3D vs. 2D computational pathology, we remove the subjectivity introduced by human interpretation. Such human-observer studies would require a significantly larger cohort of patients and a large panel of pathologists to mitigate interobserver discordance.

Previous studies have used 3D imaging of *in vitro* cancer models to examine tumorigenesis, drug response, and cancer-associated alterations in cellular development[48–50]. However, to our knowledge, this is the first report to analyze the prognostic significance of nuclei within their native 3D context in human cancer specimens. Given the relatively small number of cases in this preliminary analysis, we limited the number of 3D nuclear features to those that we deemed would most likely have prognostic significance based on previous studies[22–28, 31,51–56]. Shape-based nuclear features are an attractive choice for several reasons: they are the most frequently used features for prognostication based on 2D whole slide images[18–23, 42, 43], they are intuitive for clinical and biological interpretation[57], and there are relatively straightforward analogs between 2D and 3D shape-based features.

Our analysis shows that for PCa, epithelial nuclei hold the most prognostic significance for stratifying patients based on known clinical outcomes (Fig. 4A). Given that PCa is typically a disease of epithelial cells that form glands, this result is consistent with the underlying biology. With this set of cases and extracted features, we also find that 3D shape-based features of stromal nuclei are somewhat prognostic (Fig. 4B), which is supported by previous studies using 2D histology[27,28]. Since these stromal nuclei are from a mixture of cell types, it is not surprising that they are less prognostic than the epithelial nuclei in the cancer glands. Most importantly, for both epithelial and stromal models, our results demonstrate that 3D shape-based nuclear features are more strongly associated with BCR compared to their 2D counterparts for risk stratification (Fig. 4A, B, C, D). This finding provides additional evidence supporting the value of 3D digital pathology methods for clinical management of PCa. Further, as described in the

Results, even with the limited number of samples and extracted features in this preliminary analysis, certain differences between nuclei in indolent and aggressive cases are only statistically significant when examined in 3D vs. 2D (Fig. 4E, F).

As shown in **Supplementary Fig. 6**, significant differences in the heterogeneity (variance) for many shape-based nuclear features are observed in aggressive vs. non-aggressive cases, which is in agreement with prior 2D studies showing that nuclear shape heterogeneity is an important prognostic biomarker in PCa[22–27, 58,59]. These findings are in their early stages and given the limited number of cases examined in this report, warrant further analysis with larger patient cohorts to fully elucidate the relationships between 3D nuclear morphologies and PCa outcomes.

In this initial analysis, we have deliberately focused on a limited set of intuitive shape-based features to show that 3D nuclear features have clear prognostic value, even without exhaustively mining a large set of possible features. In other words, with some effort, we believe that better 3D features and models can be developed in the future. Note that for the analysis of sub-nuclear features, higher-resolution datasets will need to be acquired in the future, such as with the more-recent OTLS microscopy systems that have been developed[16,17].

In addition to nuclear and glandular features, there are clear opportunities to extend our work. For example, combining 3D features from diverse tissue structures, along with 3D nuclear features, could reveal novel signatures of aggressiveness. Having a comprehensive spatial and molecular view of tumors in 3D would also be of obvious clinical value[60,61]. The results of this preliminary study motivate many future exploratory directions in computational 3D pathology, as well as larger-scale clinical studies to guide treatment decisions, such as deciding which PCa patients should be placed on active surveillance vs. treated with surgery/radiation, or which patients should receive adjuvant therapies after surgery/radiation. Ultimately, we aim to demonstrate that computational 3D pathology can improve the long-term outcomes and quality of life for patients with PCa and many other diseases.

# Declarations

# Disclaimer

Any opinions, findings, and conclusions or recommendations expressed in this material are those of the authors and do not necessarily reflect the views of the NIH, NSF, Prostate Cancer Foundation, Prostate Cancer United Kingdom (PCUK) charity, Department of Defense, the Department of Veterans Affairs, or the United States Government.

# Authors' Contributions

R. Serafin: Conceptualization, data curation, software, formal analysis, investigation, visualizations, methodology, writing original manuscript. C. Koyuncu: Software, formal analysis, visualizations, writing-review and editing. W. Xie: software, data curation, writing-review and editing. H. Huang: tissue

preparation and data collection. **A. K. Glaser**: methodology, writing-review and editing. **N. P. Reder**: data curation, supervision, writing-review and editing. **A. Janowczyk**: investigation, formal analysis, methodology, writing-review and editing. **L. D. True**: Conceptualization, data curation, formal analysis, supervision, funding acquisition, investigation, writing-review and editing. **A. Matabhushi**: Resources, formal analysis, supervision, funding acquisition, methodology, investigation, writing-review and editing. **J. T. C. Liu**: Conceptualization, formal analysis, supervision, visualizations, funding acquisition, investigation, methodology, writing original manuscript, project administration, writing-review and editing.

# Data Availability

The datasets used during the current study are available from the corresponding author upon reasonable request.

# Author Conflicts

A.K. Glaser is a cofounder of Alpenglow Biosciences, Inc. N.P. Reder is a cofounder and CEO of Alpenglow Biosciences, Inc. A. Janowczyk reports personal fees from Roche, Merck, and personal fees from Lunaphore outside the submitted work. L.D. True is a cofounder of Alpenglow Biosciences, Inc. A. Madabhushi is an equity holder in Picture Health, Elucid Bioimaging, and Inspirata Inc. Currently he serves on the advisory board of Picture Health, Aiforia Inc, and SimBioSys. He also currently consults for Biohme, SimBioSys and Castle Biosciences. He also has sponsored research agreements with AstraZeneca, Boehringer-Ingelheim, Eli-Lilly and Bristol Myers-Squibb. His technology has been licensed to Picture Health and Elucid Bioimaging. He is also involved in 3 different R01 grants with Inspirata Inc. J.T.C. Liu is a cofounder and board member of Alpenglow Biosciences, Inc., which has licensed the OTLS microscopy portfolio developed in his lab at the University of Washington. No disclosures were reported by the other authors.

# References

1. Siegel, R. L., Miller, K. D., Fuchs, H. E. & Jemal, A. Cancer Statistics, 2021. *CA. Cancer J. Clin.* **71**, 7–33 (2021).

2. Egevad, L., Delahunt, B., Srigley, J. R. & Samaratunga, H. International Society of Urological Pathology (ISUP) grading of prostate cancer - An ISUP consensus on contemporary grading. APMIS **124**, 433–435 (2016).

3. Srigley, J. R. *et al.* One is the new six: The International Society of Urological Pathology (ISUP) patient-focused approach to Gleason grading. Can. Urol. Assoc. J. **10**, 339 (2016).

4. van Leenders, G. J. L. H. *et al.* The 2019 International Society of Urological Pathology (ISUP) Consensus Conference on Grading of Prostatic Carcinoma. *Am. J. Surg. Pathol.* **44**, e87–e99 (2020).

5. Shah, R. B. *et al.* Diagnosis of Gleason Pattern 5 Prostate Adenocarcinoma on Core Needle Biopsy: An Interobserver Reproducibility Study Among Urologic Pathologists. Am. J. Surg. Pathol. **39**, 1242–1249 (2015).

6. Kweldam, C. F. *et al.* Gleason grade 4 prostate adenocarcinoma patterns: an interobserver agreement study among genitourinary pathologists. Histopathology **69**, 441–449 (2016).

7. McKenney, J. K. *et al.* The Potential Impact of Reproducibility of Gleason Grading in Men With Early Stage Prostate Cancer Managed by Active Surveillance: A Multi-Institutional Study. J. Urol. **186**, 465–469 (2011).

8. Zhou, M. *et al.* Diagnosis of "Poorly Formed Glands" Gleason Pattern 4 Prostatic Adenocarcinoma on Needle Biopsy: An Interobserver Reproducibility Study Among Urologic Pathologists With Recommendations. Am. J. Surg. Pathol. **39**, 1331–1339 (2015).

9. Etzioni, R. *et al.* Overdiagnosis due to prostate-specific antigen screening: lessons from U.S. prostate cancer incidence trends. J. Natl. Cancer Inst. **94**, 981–990 (2002).

10. Renier, N. *et al.* iDISCO: A Simple, Rapid Method to Immunolabel Large Tissue Samples for Volume Imaging. Cell **159**, 896–910 (2014).

11. Susaki, E. A. *et al.* Advanced CUBIC protocols for whole-brain and whole-body clearing and imaging. Nat. Protoc. **10**, 1709–1727 (2015).

12. Azaripour, A. *et al.* A survey of clearing techniques for 3D imaging of tissues with special reference to connective tissue. Prog. Histochem. Cytochem. **51**, 9–23 (2016).

13. Power, R. M. & Huisken, J. A guide to light-sheet fluorescence microscopy for multiscale imaging. Nat. Methods **14**, 360–373 (2017).

14. Glaser, A. K. *et al.* Light-sheet microscopy for slide-free non-destructive pathology of large clinical specimens. Nat. Biomed. Eng. **1**, 0084 (2017).

15. Glaser, A. K. *et al.* Multi-immersion open-top light-sheet microscope for high-throughput imaging of cleared tissues. Nat. Commun. **10**, 2781 (2019).

16. Barner, L. A., Glaser, A. K., Huang, H., True, L. D. & Liu, J. T. C. Multi-resolution open-top light-sheet microscopy to enable efficient 3D pathology workflows. Biomed. Opt. Express **11**, 6605 (2020).

17. Glaser, A. K. *et al.* A hybrid open-top light-sheet microscope for versatile multi-scale imaging of cleared tissues. Nat. Methods **19**, 613–619 (2022).

18. Reder, N. P. *et al.* Open-Top Light-Sheet Microscopy Image Atlas of Prostate Core Needle Biopsies. Arch. Pathol. Lab. Med. **143**, 1069–1075 (2019).

19. Xie, W. *et al.* Prostate Cancer Risk Stratification via Nondestructive 3D Pathology with Deep Learning–Assisted Gland Analysis. Cancer Res. **82**, 334–345 (2022).

20. Liu, J. T. C. *et al.* Harnessing non-destructive 3D pathology. Nat. Biomed. Eng. **5**, 203–218 (2021).

21. Hawley, S. *et al.* A Model for the Design and Construction of a Resource for the Validation of Prognostic Prostate Cancer Biomarkers: The Canary Prostate Cancer Tissue Microarray. Adv. Anat. Pathol. **20**, 39–44 (2013).

22. van der Poel, H. G., Oosterhof, G. O. N., Schaafsma, H. E., Debruyne, F. M. J. & Schalken, J. A. Intratumoral nuclear morphologic heterogeneity in prostate cancer. Urology **49**, 652–657 (1997).

23. Leo, P. *et al.* Stable and discriminating features are predictive of cancer presence and Gleason grade in radical prostatectomy specimens: a multi-site study. Sci. Rep. **8**, 14918 (2018).

24. Ji, M.-Y. *et al.* Nuclear shape, architecture and orientation features from H&E images are able to predict recurrence in node-negative gastric adenocarcinoma. J. Transl. Med. **17**, 92 (2019).

25. Lee, G. *et al.* Nuclear Shape and Architecture in Benign Fields Predict Biochemical Recurrence in Prostate Cancer Patients Following Radical Prostatectomy: Preliminary Findings. Eur. Urol. Focus **3**, 457–466 (2017).

26. Carleton, N. M., Lee, G., Madabhushi, A. & Veltri, R. W. Advances in the computational and molecular understanding of the prostate cancer cell nucleus. J. Cell. Biochem. **119**, 7127–7142 (2018).

27. Chandramouli, S. *et al.* Computer Extracted Features from Initial H&E Tissue Biopsies Predict Disease Progression for Prostate Cancer Patients on Active Surveillance. Cancers **12**, 2708 (2020).

28. Bhargava, H. K. *et al.* Computationally Derived Image Signature of Stromal Morphology Is Prognostic of Prostate Cancer Recurrence Following Prostatectomy in African American Patients. Clin. Cancer Res. **26**, 1915–1923 (2020).

29. Zwerger, M., Ho, C. Y. & Lammerding, J. Nuclear mechanics in disease. Annu. Rev. Biomed. Eng. **13**, 397–428 (2011).

30. Martins, R. P., Finan, J. D., Guilak, F. & Lee, D. A. Mechanical regulation of nuclear structure and function. Annu. Rev. Biomed. Eng. **14**, 431–455 (2012).

31. Zink, D., Fischer, A. H. & Nickerson, J. A. Nuclear structure in cancer cells. Nat. Rev. Cancer **4**, 677–687 (2004).

32. Schreiber, K. H. & Kennedy, B. K. When lamins go bad: nuclear structure and disease. Cell **152**, 1365–1375 (2013).

33. Nickerson, J. A., Blencowe, B. J. & Penman, S. The architectural organization of nuclear metabolism. Int. Rev. Cytol. **162A**, 67–123 (1995).

34. Stringer, C., Wang, T., Michaelos, M. & Pachitariu, M. Cellpose: a generalist algorithm for cellular segmentation. Nat. Methods **18**, 100–106 (2021).

35. Pietzsch, T., Saalfeld, S., Preibisch, S. & Tomancak, P. BigDataViewer: visualization and processing for large image data sets. Nat. Methods **12**, 481–483 (2015).

36. Hörl, D. *et al.* BigStitcher: reconstructing high-resolution image datasets of cleared and expanded samples. Nat. Methods **16**, 870–874 (2019).

37. Serafin, R., Xie, W., Glaser, A. K. & Liu, J. T. C. FalseColor-Python: A rapid intensity-leveling and digital-staining package for fluorescence-based slide-free digital pathology. PLOS ONE **15**, e0233198 (2020).

38. van der Walt, S. *et al.* scikit-image: image processing in Python. PeerJ **2**, e453 (2014).

39. King, C. R. & Long, J. P. Prostate biopsy grading errors:A sampling problem? Int. J. Cancer **90**, 326–330 (2000).

40. Tibshirani, R. Regression Shrinkage and Selection Via the Lasso. J. R. Stat. Soc. Ser. B Methodol. **58**, 267–288 (1996).

41. Kuhn, M. & Johnson, K. *Applied predictive modeling*. (Springer, 2013).

42. Stephenson, A. J. *et al.* Postoperative Nomogram Predicting the 10-Year Probability of Prostate Cancer Recurrence After Radical Prostatectomy. J. Clin. Oncol. **23**, 7005–7012 (2005).

43. Virtanen, P. *et al.* SciPy 1.0: fundamental algorithms for scientific computing in Python. Nat. Methods **17**, 261–272 (2020).

44. Leo, P. *et al.* Computer extracted gland features from H&E predicts prostate cancer recurrence comparably to a genomic companion diagnostic test: a large multi-site study. Npj Precis. Oncol. **5**, 35 (2021).

45. Leo, P. *et al.* Computationally Derived Cribriform Area Index from Prostate Cancer Hematoxylin and Eosin Images Is Associated with Biochemical Recurrence Following Radical Prostatectomy and Is Most Prognostic in Gleason Grade Group 2. Eur. Urol. Focus **7**, 722–732 (2021).

46. Cooperberg, M. R. *et al.* Multiinstitutional validation of the UCSF cancer of the prostate risk assessment for prediction of recurrence after radical prostatectomy. Cancer **107**, 2384–2391 (2006).

47. Newcomb, L. F. *et al.* Outcomes of Active Surveillance for Clinically Localized Prostate Cancer in the Prospective, Multi-Institutional Canary PASS Cohort. J. Urol. **195**, 313–320 (2016).

48. Roberge, C. L. *et al.* Non-Destructive Tumor Aggregate Morphology and Viability Quantification at Cellular Resolution, During Development and in Response to Drug. Acta Biomater. **117**, 322–334 (2020).

49. Kingsley, D. M. *et al.* Laser-based 3D bioprinting for spatial and size control of tumor spheroids and embryoid bodies. Acta Biomater. **95**, 357–370 (2019).

50. Wen, Y. *et al.* Quantitative analysis and comparison of 3D morphology between viable and apoptotic MCF-7 breast cancer cells and characterization of nuclear fragmentation. PLOS ONE **12**, e0184726 (2017).

51. Nickerson, J. A. Nuclear dreams: The malignant alteration of nuclear architecture. J. Cell. Biochem. **70**, 172–180 (1998).

52. Uhler, C. & Shivashankar, G. V. Nuclear Mechanopathology and Cancer Diagnosis. Trends Cancer **4**, 320–331 (2018).

53. Bhargava, R. & Madabhushi, A. Emerging Themes in Image Informatics and Molecular Analysis for Digital Pathology. Annu. Rev. Biomed. Eng. **18**, 387–412 (2016).

54. Hveem, T. S. *et al.* Chromatin changes predict recurrence after radical prostatectomy. Br. J. Cancer **114**, 1243–1250 (2016).

55. Lee, G. *et al.* Cell Orientation Entropy (COrE): Predicting Biochemical Recurrence from Prostate Cancer Tissue Microarrays. in *Medical Image Computing and Computer-Assisted Intervention – MICCAI 2013* (eds. Mori, K., Sakuma, I., Sato, Y., Barillot, C. & Navab, N.) vol. 8151 396–403 (Springer Berlin Heidelberg, 2013).

56. Ali, S., Veltri, R., Epstein, J. A., Christudass, C. & Madabhushi, A. Cell cluster graph for prediction of biochemical recurrence in prostate cancer patients from tissue microarrays. in (eds. Gurcan, M. N. & Madabhushi, A.) 86760H (2013). doi:10.1117/12.2008695.

57. Fischer, E. G. Nuclear Morphology and the Biology of Cancer Cells. Acta Cytol. **64**, 511–519 (2020).

58. Veltri, R. W., Isharwal, S., Miller, M. C., Epstein, J. I. & Partin, A. W. Nuclear roundness variance predicts prostate cancer progression, metastasis, and death: A prospective evaluation with up to 25 years of follow-up after radical prostatectomy. *The Prostate* n/a-n/a (2010) doi:10.1002/pros.21168.

59. Veltri, R. W. & Christudass, C. S. Nuclear Morphometry, Epigenetic Changes, and Clinical Relevance in Prostate Cancer. in *Cancer Biology and the Nuclear Envelope* (eds. Schirmer, E. C. & de las Heras, J. I.) vol. 773 77–99 (Springer New York, 2014).

60. Lewis, S. M. *et al.* Spatial omics and multiplexed imaging to explore cancer biology. Nat. Methods **18**, 997–1012 (2021).

61. Berger, M. F. & Mardis, E. R. The emerging clinical relevance of genomics in cancer medicine. Nat. Rev. Clin. Oncol. **15**, 353–365 (2018).
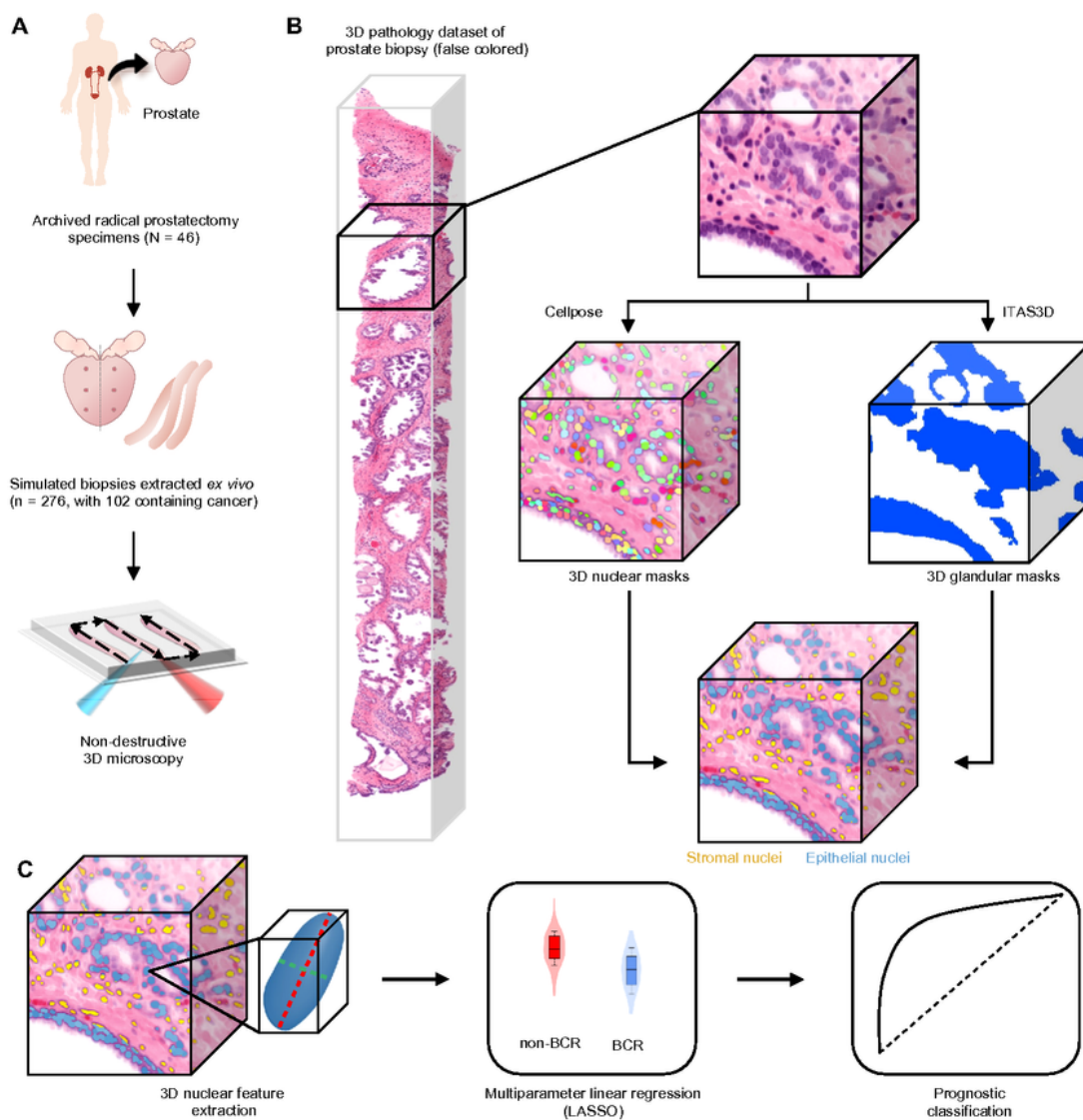
# Figures

Figure 1

**Workflow to evaluate the prognostic value of 3D nuclear features for prostate cancer risk assessment.** (A) Archived (FFPE) radical prostatectomy specimens were obtained from a 46-patient cohort with known 5-year biochemical recurrence (BCR) outcomes, from which simulated (ex vivo) biopsies were extracted (6 biopsies per case, per sextant biopsy protocol). The biopsies were labeled with a fluorescent analog of H&E, optically cleared to render them transparent to light, and comprehensively imaged in 3D via OTLS

microscopy. (B) 3D nuclear segmentation masks of cancer-containing regions were generated using the deep-learning based cellpose model and 3D glandular segmentations were generated by the previously published ITAS3D pipeline. This enabled us to distinguish between nuclei in the glandular epithelium (blue) versus the surrounding stroma (yellow). (C) 3D shape-based features of epithelial and stromal nuclei were extracted and passed into a multiparameter classifier (LASSO) to stratify patients based on 5-year BCR outcomes.
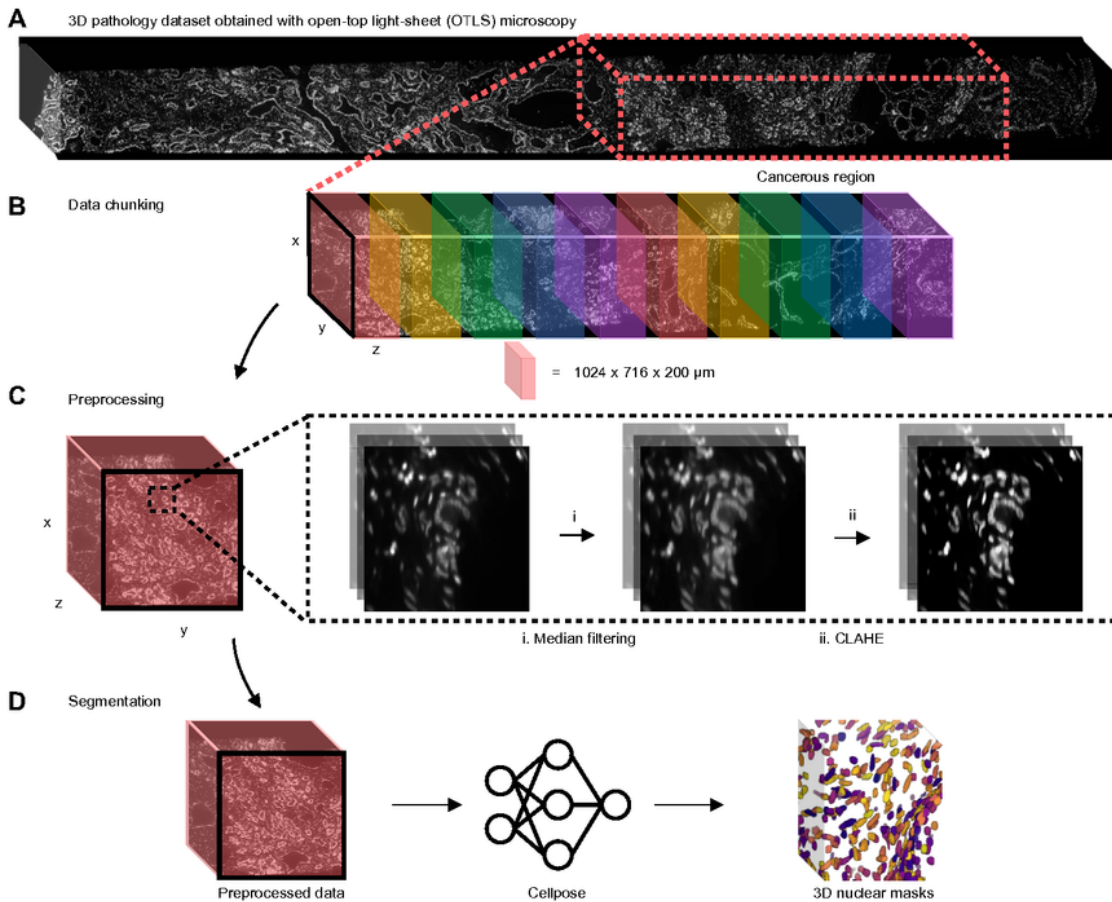
**A** 3D pathology dataset obtained with open-top light-sheet (OTLS) microscopy

Cancerous region

**B** Data chunking

x

y

z

= 1024 x 716 x 200 µm

**C** Preprocessing

x

z

y

i

ii

i. Median filtering

ii. CLAHE

**D** Segmentation

Preprocessed data

Cellpose

3D nuclear masks

# Figure 2

**3D nuclear segmentation pipeline for biopsies imaged with OTLS microscopy. (A)** Nuclear channel (To-Pro-3) of a PCa biopsy imaged by OTLS microscopy with the cancerous region outlined with a dashed red box. **(B)** The cancerous region is broken up into discrete data chunks before processing. **(C)** Each data chunk is passed into a two-step preprocessing procedure before segmentation (see text for details). **(D)**

Preprocessed data chunks are passed into cellpose to generate 3D nuclear segmentation masks, where each segmented nucleus is assigned a unique label.
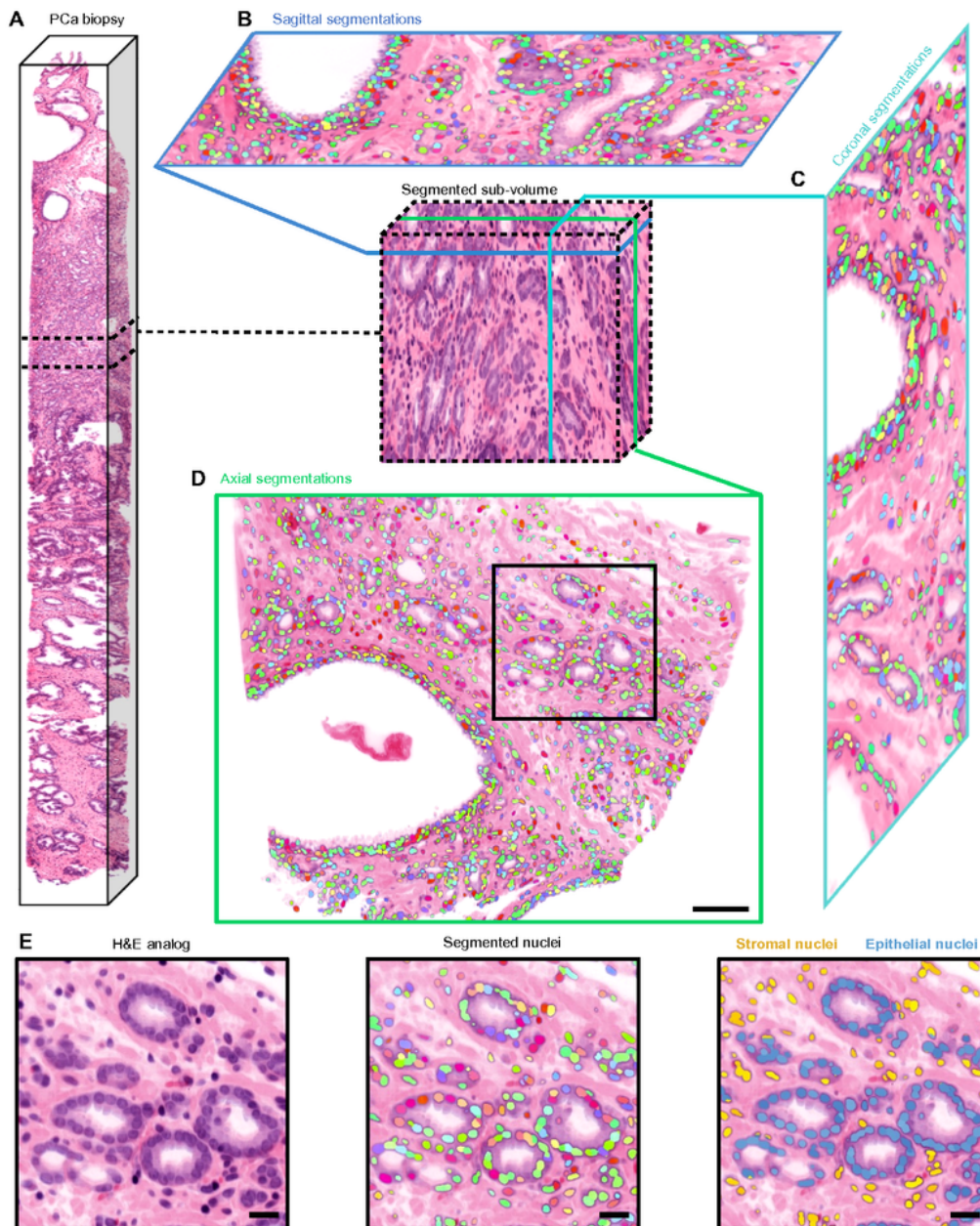


**Figure 3**

**Image atlas of 3D nuclear segmentation results.** **(A)** Non-destructive 3D pathology dataset of a PCa biopsy and segmented sub-volume. Sagittal **(B),** coronal **(C)**, and axial **(D)** views of 3D nuclear

segmentations of the segmented sub-volume. During segmentation, each identified nucleus is given a unique integer label, which is represented by a color for visualization purposes (scale bar = 100 µm). **(E)** Larger field of view showing cancerous glands and surrounding stroma (left). colorized segmentation masks overlaid onto H&E false-colored OTLS images (middle). Segmented nuclei colored by their location within the prostate microarchitecture (right) (scale bar = 50 µm).
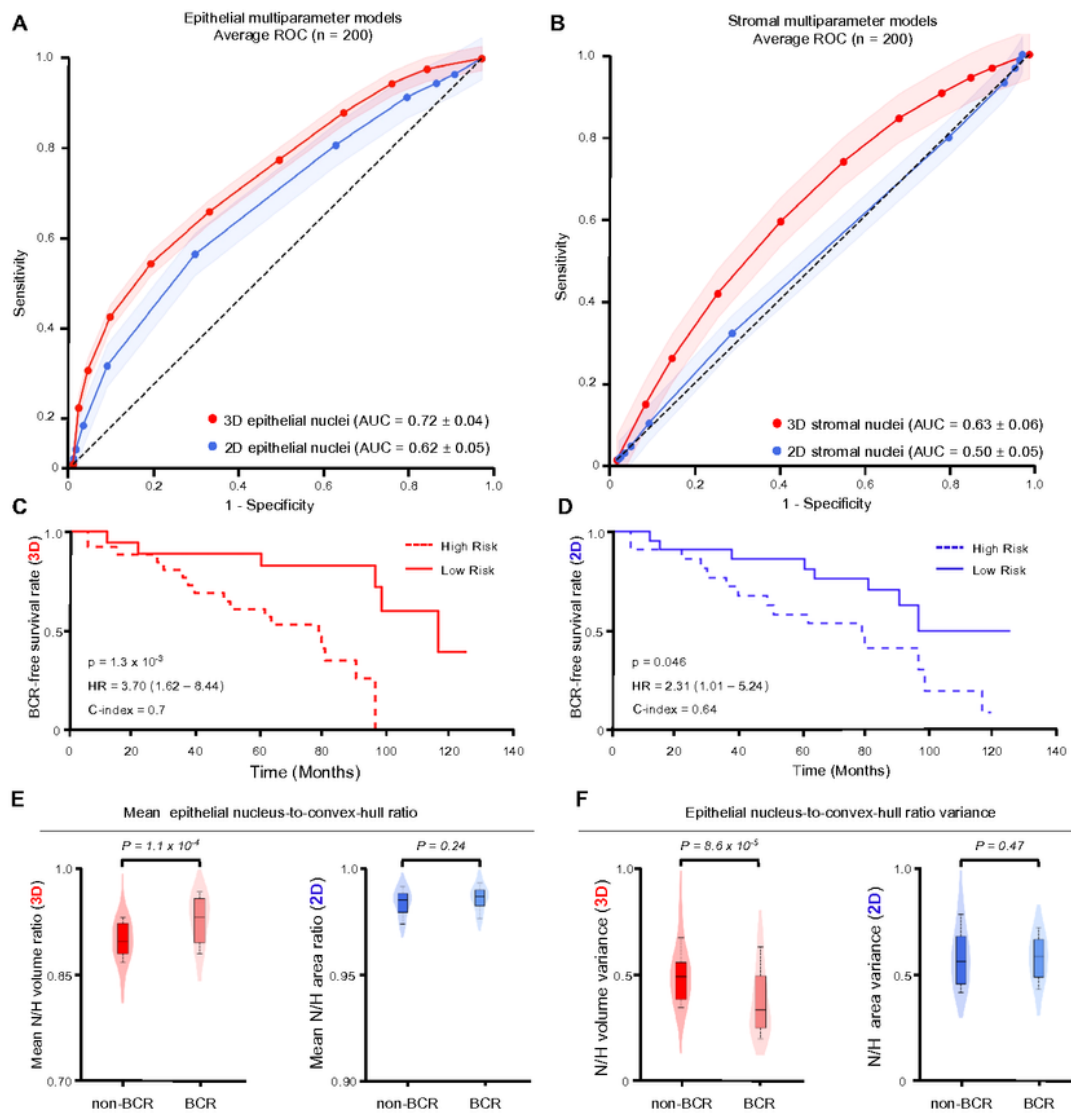


**Figure 4**

Clinical analysis comparing the prognostic value of 3D & 2D nuclear features. (A) ROC curves are shown for multiparameter models trained on 3D (red) and 2D (blue) nuclear features in epithelial regions. (B) ROC curves of multiparameter models trained on 3D (red) and 2D (blue) nuclear features in stromal regions. (C, D) KM curves are shown for BCR-free survival, showing that the model trained on epithelial 3D nuclear features (C) can better stratify patients into low- and high-risk categories than the model trained on epithelial 2D nuclear features (D). (E, F) Violin and box plots are shown for two examples of epithelial 3D nuclear features, along with their analogous 2D features, for cases in which BCR occurred within 5 years of radical prostatectomy ("BCR") and for cases in which there was no BCR within 5 years of radical prostatectomy ("non-BCR"). For both example features, "Mean epithelial nucleus-to-convex-hull ratio" in (E), and "epithelial nucleus-to-convex-hull variance" in (F), the 3D feature shows improved patient risk stratification compared to its 2D counterpart.

## Supplementary Files

This is a list of supplementary files associated with this preprint. Click to download.

- SupplementaryMaterials.docx
- supplementaryvideo1.avi
- supplementaryvideo2.mp4
- supplementaryvideo3.avi